

Proposal for measuring out-of-time-ordered correlators at finite temperature with coupled spin chains

Bhuvanesh Sundar^{1,2}, Andreas Elben^{2,3,4}, Lata Kh Joshi^{2,3}, and Torsten V. Zache^{2,3}

¹JILA, Department of Physics, University of Colorado, Boulder, CO 80309, USA

²Institute for Quantum Optics and Quantum Information of the Austrian Academy of Sciences, Innsbruck A-6020, Austria

E-mail: bhuvanesh.sundar@colorado.edu

³Center for Quantum Physics, University of Innsbruck, Innsbruck A-6020, Austria

⁴Institute for Quantum Information and Matter and Walter Burke Institute for Theoretical Physics, California Institute of Technology, Pasadena, CA 91125, USA

Abstract. Information scrambling, which is the spread of local information through a system's many-body degrees of freedom, is an intrinsic feature of many-body dynamics. In quantum systems, the out-of-time-ordered correlator (OTOC) quantifies information scrambling. Motivated by experiments that have measured the OTOC at infinite temperature and a theory proposal to measure the OTOC at finite temperature using the thermofield double state, we describe a protocol to measure the OTOC in a finite temperature spin chain that is realized approximately as one half of the ground state of two moderately-sized coupled spin chains. We consider a spin Hamiltonian with particle-hole symmetry, for which we show that the OTOC can be measured without needing sign-reversal of the Hamiltonian. We describe a protocol to mitigate errors in the estimated OTOC, arising from the finite approximation of the system to the thermofield double state. We show that our protocol is also robust to main sources of decoherence in experiments.

1. Introduction

Present day quantum simulators based on trapped ions [1, 2], ultracold ground state atoms [3] and Rydberg atoms [4], and other platforms [5–8] provide unique opportunities to study the time evolution of quantum many-body systems in a controlled laboratory setting. In atomic physics, analog quantum simulators with ultracold atoms in deep optical lattices realize effective spin models with nearest-neighbor interactions [3, 9–12], and simulators with Rydberg tweezer arrays or trapped ion chains realize spin models with longer ranged interactions [13–17]. These experiments have several control parameters which allow one to controllably modify, or even completely turn off, these interactions, for example by increasing the lattice depth in optical lattices or detuning the atomic levels in Rydberg systems. This flexibility, and the ability to

imprint local operations and make measurements, pave the way to develop quantum algorithms for measuring quantitative probes of the system's non-equilibrium dynamics and thermalization.

A fundamental question in out-of-equilibrium many-body dynamics is how quantum systems thermalize and scramble information. We describe a protocol to measure a system's finite-temperature out-of-time-ordered correlation (OTOC), which quantifies the nature of information scrambling, and which we will further describe in detail below. Our method is geared towards analog quantum simulators which realize particle-hole symmetric Hamiltonians that satisfy the eigenstate thermalization hypothesis (ETH). As a concrete example, we consider a long-ranged XX model that can be implemented with Rydberg atoms. We propose to measure the OTOC for this system by evolving the thermofield double state initially prepared approximately on coupled spin chains. The thermofield double state on two chains realizes a finite temperature system on each chain, and can be prepared relatively easily in systems that satisfy ETH [18]. Particle-hole symmetry yields a favorable scenario where, as we will explain, our protocol measures the OTOC without challenging requirements such as reversing the Hamiltonian's sign.

Information scrambling, which is the spread of local information through a system's degrees of freedom, is an intrinsic feature of many-body dynamics [19, 20]. In quantum systems, the effects of scrambling on an initially local operator V are reflected in the Heisenberg time evolution with an underlying Hamiltonian H , i.e., $V(t) = \exp(iHt/\hbar)V(0)\exp(-iHt/\hbar)$. One way to quantify this spread is through the square of the commutator of $V(t)$ with another local operator $W(0)$, i.e., $C(t) = \langle [V(t), W(0)]^2 \rangle$. Here, the expectation value is taken in the thermal state $\rho_\beta = \exp(-\beta H)/Z$, with $Z = \text{tr}(\exp(-\beta H))$ and β denotes the inverse temperature, $\beta = 1/(k_B T)$. OTOCs, which we are interested in, are two of the four terms in the expansion of $C(t)$, namely $\langle W^\dagger(0)V^\dagger(t)W(0)V(t) \rangle$ and $\langle V^\dagger(t)W^\dagger(0)V(t)W(0) \rangle$.

The OTOC serves as a crucial observable to understand information scrambling in quantum systems [19, 21–30]. Generically, OTOCs decay with time until $V(t)$ has reached all the degrees of freedom, in a time scale known as the scrambling time, t_{scr} . The scaling of t_{scr} with system size diagnoses how fast or slow the system scrambles information. The decay time and nature of spreading (e.g., diffusive or ballistic) can depend on parameters in the Hamiltonian [30–35] or state properties like the temperature (T) [36–38]. In addition to characterizing the nature of scrambling, OTOCs can also be used to diagnose quantum phase transitions [39–47]. Due to their fundamental importance in information scrambling and other applications listed above, there has been enormous interest in measuring OTOCs in recent years.

There are previous theoretical proposals to experimentally measure OTOCs in the infinite temperature state [41, 48, 49]. Some of them involve time evolution by reversing the Hamiltonian's sign [50], or by controlling the Hamiltonian's sign with an ancillary qubit which acts as a switch [51, 52]. Proposals to measure OTOCs without reversing time evolution involve implementing the SWAP operator between two systems either as an ensemble of random initial states [48] or in the measurement [53], or by making

weak measurements [54]. These methods have been used in experiments to measure the OTOC in nuclear magnetic resonance simulators [55–57], trapped ions [58–60] and superconducting qubits [61].

Refs. [48, 49] describe how to extend the infinite-temperature methods discussed there to measure the OTOC at finite temperature (referred to as thermal OTOC). Other proposals to measure the thermal OTOC consider two copies of the same system in an entangled initial state prepared at a negative time [62], or two copies of the system sampled from a thermal ensemble [53]. However, despite these proposals, the OTOC at a finite temperature has not been measured in experiments.

In this work, we describe how to measure the thermal OTOC in analog quantum simulators, without initial state preparation at negative times or the need to evolve backward in time, for systems satisfying ETH and with particle-hole symmetry. Our method is inspired by ideas to prepare the thermofield double state in [18, 63], and measure the thermal OTOC from the thermofield double state [62, 63]. We consider a concrete example – a 1D spin model with long-ranged XX interactions – that can be implemented in state-of-the-art atomic simulators [13]. We also show how to measure the OTOC in experiments in the presence of limitations due to non-ideal dynamics as well as systematic limitations of the measurement protocol. A similar method that measures the OTOC at infinite temperature was proposed in [64].

This article is organized as follows. In Section 2, we review the thermofield double (TFD) state and show how it can be used to measure thermal OTOCs. In Section 3, we numerically show how to approximately access the TFD for a 1D spin Hamiltonian as the ground state of a local parent Hamiltonian on two coupled spin chains. In Section 4, we numerically show that an approximation to the OTOC can be measured from the ground state described in Section 3, and describe a correction protocol to mitigate the error in this approximation. In Section 5, we numerically show that our correction protocol also mitigates errors that arise from decoherence in experiment. In Section 6, we discuss connections between our protocol and previous proposals to measure the OTOC. We summarize in Section 7.

2. O_{th} from Thermofield Double state

There are different regularized versions of the thermal OTOC in the literature [23, 53, 62]. Here, we consider the following thermal OTOC between operators W and V ,

$$O_{th}(\beta, t) = \frac{\text{tr}(e^{-\beta H/2} W^\dagger V^\dagger(t) W e^{-\beta H/2} V(t))}{Z}. \quad (1)$$

In Appendix A, we state the other definitions of the thermal OTOC and explore their temperature dependence for the model considered in this paper.

The TFD state at temperature $T \equiv 1/(k_B \beta)$ is an entangled state on $2n$ qubits (for an n -qubit Hamiltonian), defined as

$$|\text{tfd}(\beta)\rangle = \frac{\sum_E e^{-\beta E/2} |E\rangle \otimes |E^*\rangle}{\sqrt{Z}}. \quad (2)$$

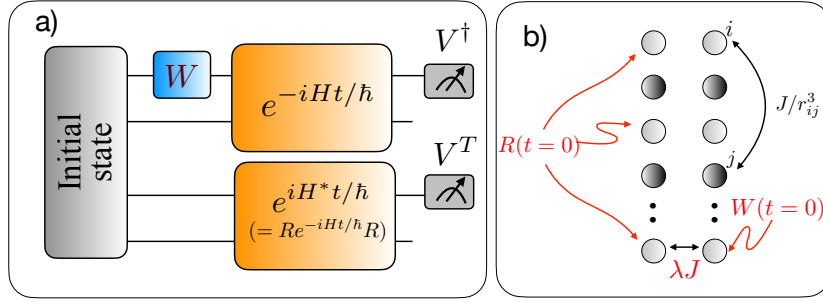


Figure 1. (a) Schematic of the protocol to measure the OTOC. We propose to initialize the system in the thermofield double state $|\text{tfd}(\beta)\rangle$ in the exact protocol, and in the ground state $|g(\lambda)\rangle$ of H_{parent} in the experimentally feasible protocol, which closely approximates $|\text{tfd}(\beta)\rangle$ up to a symmetry operation (see main text). Then, we apply $W \otimes 1$, and evolve the two halves independently with H and $-H^*$ respectively. For the example we consider [see (b)], $-H^* = RHR$ can be realized by implementing unitary single-qubit gates R before and after time evolution with H . Measuring $V^\dagger \otimes V^T$ gives O_{th} in the exact protocol, and $O_g \sim O_{\text{th}}$ in the experimental case [see (13)]. Performing an identical experiment with $W = 1$ gives N_g . The corrected estimate for the OTOC is $O_{\text{corr}} = O_g/N_g$ [(14)]. (b) Schematic of the physical setup. We consider qubits on a $2 \times n$ ladder, with long-range intra-leg interactions given by J/r_{ij}^3 [see (7)], and inter-leg interactions given by λJ [(9)] which sets the effective temperature. The intra-leg Hamiltonian was recently realized in [13]. The initial state is prepared at $t = 0$, the inter-leg coupling λ is turned off and $W \otimes R$ is applied at $t = 0$, and the two legs are evolved independently for $t > 0$.

The sum in (2) runs over the eigenstates $|E\rangle$ of H , with respective eigenvalues E , i.e., $H|E\rangle = E|E\rangle$. We denote H^* and $|E^*\rangle$ as the complex conjugates of H and $|E\rangle$, satisfying $H^*|E^*\rangle = E|E^*\rangle$. Preparing $|\text{tfd}(\beta)\rangle$, which is a highly entangled state, in an experiment is non-trivial and is an active area of research. One technique that has been successfully used in the past uses variational quantum circuits [65, 66]. Here, we show that O_{th} can be measured if one can access $|\text{tfd}(\beta)\rangle$.

In an ideal situation where an experiment can access $|\text{tfd}(\beta)\rangle$, Figure 1(a) shows a circuit for measuring $O_{\text{th}}(\beta, t)$. After preparing the initial state $|\text{tfd}(\beta)\rangle$, we apply $W \otimes 1$ which prepares $|\psi_W(\beta, 0)\rangle = (W \otimes 1)|\text{tfd}(\beta)\rangle$. We then evolve the system with $H \otimes 1 - 1 \otimes H^*$ for a time t , and measure $V^\dagger \otimes V^T$, leading to,

$$O_{\text{tfd}}(\beta, t) = \langle \psi_W(\beta, t) | V^\dagger \otimes V^T | \psi_W(\beta, t) \rangle. \quad (3)$$

Here, $|\psi_W(\beta, t)\rangle = \exp(-i(H_1 - H_2^*)t/\hbar) |\psi_W(\beta, 0)\rangle$, where we denote $H_1 = H \otimes 1$ and $H_2 = 1 \otimes H$. This protocol requires evolving qubits $[n+1, 2n]$ with $-H^*$.

The measurement $O_{\text{tfd}}(\beta, t)$ in (3) is equal to the thermal OTOC $O_{\text{th}}(\beta, t)$ in (1). This can be seen from

$$\begin{aligned} O_{\text{tfd}}(\beta, t) &= \langle \text{tfd}(\beta) | (W^\dagger \otimes 1) e^{i(H_1 - H_2^*)t/\hbar} (V^\dagger \otimes V^T) e^{-i(H_1 - H_2^*)t/\hbar} (W \otimes 1) | \text{tfd}(\beta) \rangle \\ &= \sum_{EE'} \frac{e^{-\beta(E+E')/2}}{\text{tr } e^{-\beta H}} \langle E' | W^\dagger e^{iHt/\hbar} V^\dagger e^{-iHt/\hbar} W | E \rangle \langle E'^* | e^{-iH^*t/\hbar} V^T e^{iH^*t/\hbar} | E^* \rangle \end{aligned}$$

$$\begin{aligned}
 &= \sum_{EE'} \frac{e^{-\beta(E+E')/2}}{\text{tr } e^{-\beta H}} \langle E' | W^\dagger e^{iHt/\hbar} V^\dagger e^{-iHt/\hbar} W | E \rangle \langle E | e^{iHt/\hbar} V e^{-iHt/\hbar} | E' \rangle \\
 &= \frac{\text{tr} (e^{-\beta H/2} W^\dagger V^\dagger(t) W e^{-\beta H/2} V(t))}{\text{tr } e^{-\beta H}} \\
 &= O_{\text{th}}(\beta, t).
 \end{aligned} \tag{4}$$

Two corollaries follow from (4). First, a straightforward substitution shows that setting $W = 1$ yields a measurement that is constant in time. This is because $|\text{tfd}(\beta)\rangle$ is an eigenstate of $H_1 - H_2^*$. We denote this special case as $N_{\text{tfd}}(\beta)$,

$$\begin{aligned}
 N_{\text{tfd}}(\beta) &= \langle \psi_{W=1}(\beta, t) | V^\dagger \otimes V^T | \psi_{W=1}(\beta, t) \rangle \\
 &= \frac{\text{tr} (e^{-\beta H/2} V^\dagger e^{-\beta H/2} V)}{\text{tr } e^{-\beta H}}.
 \end{aligned} \tag{5}$$

Second, O_{tfd} is invariant under the application of any unitary operation S to the initial state $|\text{tfd}(\beta)\rangle$ before time evolution, if the following conditions are satisfied:

$$\begin{aligned}
 [S, H_1 - H_2^*] &= 0, \\
 S(W \otimes 1) &= \pm(W \otimes 1)S, \\
 S(V^\dagger \otimes V^T) &= (V^\dagger \otimes V^T)S.
 \end{aligned} \tag{6}$$

These conditions will be important in our discussions regarding the physical implementation of the measurement protocol in the next sections.

Next, we present a protocol suitable for analog quantum simulators, inspired by earlier findings in [18, 62, 63], where we approximately prepare $|\phi(\beta)\rangle = U_0 |\text{tfd}(\beta)\rangle$ as the ground state of a local parent Hamiltonian, with U_0 satisfying the conditions in (6).

3. Approximating $|\text{tfd}(\beta)\rangle$ in an atomic quantum simulator

For a certain class of Hamiltonians – those that satisfy the eigenstate thermalization hypothesis (ETH) – the thermofield double state has a large overlap with the ground state of a local parent Hamiltonian defined on two appropriately coupled copies of the system [18]. We consider the Hamiltonian

$$H = \sum_{i \text{ even}} \sum_{j \text{ odd}} \frac{J}{r_{ij}^3} (\sigma_i^x \sigma_j^x + \sigma_i^y \sigma_j^y), \tag{7}$$

where r_{ij} is the distance between spins i and j , J is the interaction strength between neighboring spins, and the sum runs over $1 \leq i, j \leq n$ with i odd and j even. We expect that the long-range interactions will allow the system to thermalize and thus satisfy ETH. Consistent with this, we will show analytical and numerical evidence that the ground state $|g(\lambda)\rangle$ of a local parent Hamiltonian $H_{\text{parent}}(\lambda)$ on two coupled chains has a large overlap with $|\phi(\beta)\rangle = U_0 |\text{tfd}(\beta)\rangle$, for moderate system sizes $n \leq 11$. The operator U_0 should be included due to symmetry considerations that we explain below.

We chose the above Hamiltonian H for two further reasons. First, a recent experiment [13] with Rydberg atoms has realized a variant of H where the nearest-neighbor interactions are staggered, i.e. a long-range SSH model. Second, the

Hamiltonian we consider has particle-hole symmetry, which makes it straightforward to realize the time evolution with $-H^*$ in experiment, which is necessary in our protocol [see Section 2]. Particle-hole symmetry means that there exists a unitary R such that $-H^* = R^\dagger H R$, shown as a parenthetical comment in the time evolution operator in Figure 1(a). For our example, $R = \prod_{n+1 \leq k \leq 2n, k \in \text{even}} \sigma_k^z$. This is significant because it is easier to realize the evolution operator $\exp(-i(H_1 - H_2^*)t/\hbar)$ as $(1 \otimes R^\dagger) \exp(-i(H_1 + H_2)t/\hbar)(1 \otimes R)$ than by physically reversing the sign of the interactions. Some particle-hole symmetric models have relatively simple forms for R . For example, the nearest-neighbor transverse Ising model has $R_{\text{TIM}} = (\prod_{i \text{ odd}} \sigma_i^x)(\prod_{i \text{ even}} \sigma_i^z)$. However, finding and implementing such R may be infeasible for other cases. We note that particle-hole symmetry is not a requirement; depending on the experimental setup, it may be advantageous to explicitly reverse the Hamiltonian's sign in experiment.

We consider the parent Hamiltonian on two coupled spin chains,

$$H_{\text{parent}}(\lambda) = H_1 + H_2 + \lambda H_{12}. \quad (8)$$

Here, $H_1 = H \otimes 1$ is the Hamiltonian in (7) acting on spins $1 \leq k \leq n$ which comprise one leg of the ladder [see Figure 1(b)], $H_2 = 1 \otimes H$ is the Hamiltonian acting on spins $n+1 \leq k \leq 2n$ which comprise the other leg of the ladder, and H_{12} describes interactions between the two legs,

$$H_{12} = J \sum_{1 \leq k \leq n} (\sigma_k^x \sigma_{k+n}^x + \sigma_k^y \sigma_{k+n}^y). \quad (9)$$

The coupling λ can, for example, be tuned by adjusting the distance between the chains, or their orientation relative to the quantization axis.

We will demonstrate that there is large fidelity,

$$F(\beta, \lambda) = |\langle g(\lambda) | \phi(\beta) \rangle|^2, \quad (10)$$

between the ground state $|g(\lambda)\rangle$ of $H_{\text{parent}}(\lambda)$, and $|\phi(\beta)\rangle$, where

$$|\phi(\beta)\rangle = \left(\prod_{k=1}^n \sigma_k^y \right) \otimes 1 |\text{tfd}(\beta)\rangle \equiv U_0 \otimes 1 |\text{tfd}(\beta)\rangle. \quad (11)$$

Our argument consists of three steps. First, we show that $|g(\lambda)\rangle$ and $|\phi(\beta)\rangle$ have the same total azimuthal spin, which is a symmetry of the system. Then, we will show two limiting cases where $|g(\lambda)\rangle = |\phi(\beta)\rangle$ for appropriate β . Finally, we will numerically show that $F(\beta, \lambda)$ is large even for non-limiting cases, and justify this from a conformal field theory perspective. Thus, the OTOC can be approximately measured using the circuit in Figure 1, with $|g(\lambda)\rangle$ replacing $|\text{tfd}(\beta)\rangle$. We derive an upper bound for the error in the measured OTOC in terms of $F(\beta, \lambda)$, and describe a protocol to mitigate this error.

3.1. Symmetry consideration

We begin by observing that a symmetry operator for H_{parent} is the total azimuthal spin $S^z = \sum_{i=1}^{2n} \sigma_i^z$. The ground state $|g(\lambda)\rangle$ is an eigenstate of S^z with eigenvalue 0.

S^z is also a symmetry operator for H . We split $S^z = S_{(1)}^z + S_{(2)}^z$, where $S_{(i)}^z$ is the total spin in each chain. Each eigenstate $|E\rangle$ ($|E^*\rangle$) of H (H^*) is an eigenstate of $S_{(i)}^z$, therefore each term $|E\rangle \otimes |E^*\rangle$ in (2) is an eigenstate of S^z , but each has a different eigenvalue. Therefore, $|\text{tfd}(\beta)\rangle$ is generically not an eigenstate of S^z .

Instead, $|\phi(\beta)\rangle$ is an eigenstate of S^z with eigenvalue 0. This can be seen by writing $|\phi(\beta)\rangle$ as

$$|\phi(\beta)\rangle = \frac{\sum_E e^{-\beta E/2} (U_0 |E\rangle) \otimes |E^*\rangle}{\sqrt{Z}}, \quad (12)$$

with U_0 defined in (11). $U_0 |E\rangle$ and $|E\rangle^*$ are eigenstates of $S_{(i)}^z$ with eigenvalues of equal magnitude but opposite sign. Note that U_0 satisfies the first condition in (6), and satisfies the other two conditions for Pauli operators W and V . Therefore, replacing $|\text{tfd}(\beta)\rangle$ with $|\phi(\beta)\rangle$ in (4) still yields $O_{\text{th}}(\beta, t)$.

For each λ , there exists an inverse temperature $\beta_0(\lambda)$ which yields the largest overlap $F(\beta_0(\lambda), \lambda) = |\langle g(\lambda) | \phi(\beta_0(\lambda)) \rangle|^2$. In this way, tuning λ sets the temperature $T_0(\lambda) \equiv 1/(k_B \beta_0(\lambda))$ of the state. An intuitive reason to understand this is that the coupling λ determines the amount of entanglement between the two chains, and thus determines the temperature within one chain. Hereafter, we refer to $T_0(\lambda)$ as T_0 , dropping the argument λ . We find T_0 by maximizing $F(\beta, \lambda)$.

3.2. Limiting cases

$|g(\lambda)\rangle$ is exactly equal to $|\phi(\beta_0)\rangle$ in the limits $\lambda = 0$ and $\lambda = \infty$. In the limit of strongly coupled legs, $|g(\lambda = \infty)\rangle$ is a tensor product of spin singlets $(|\uparrow\downarrow\rangle - |\downarrow\uparrow\rangle)\sqrt{2}$ on each rung of the ladder, and satisfies $|g(\lambda = \infty)\rangle = |\phi(\beta_0 = 0)\rangle$, i.e. $F(0, \infty) = 1$. When $\lambda = 0$, the ladder's two legs are independent, thus $|g(\lambda = 0)\rangle$ is a tensor product of the ground state on each leg of the ladder. Then, $|g(\lambda = 0)\rangle = |\phi(\beta_0 = \infty)\rangle$, i.e. $F(\infty, 0) = 1$. Note that $|g(0)\rangle$ is an eigenstate of U_0 . Finally, $|g(\lambda)\rangle = |\phi(\beta_0)\rangle$ also for $n = 2$ and arbitrary λ [see Appendix B].

3.3. Non-limiting cases

Next, we consider finite nonzero λ . Figure 2(a) plots the maximum fidelity $F(\beta_0, \lambda)$ versus λ , and Figure 2(b) plots the temperature $T_0 = 1/(k_B \beta_0)$ where this maximum occurs. The fidelity is always $\gtrsim 88\%$ up to $n = 11$, and is smallest around $\lambda = 1$ for all n . The inset shows the scaling of $F(\beta_0, \lambda)$ with n at $\lambda = 1$. The temperature T_0 corresponding to the maximum fidelity smoothly increases with λ and varies with n . We extrapolate T_0 to $n = \infty$, by fitting a straight line to T_0 versus $1/n$ as shown in the inset of Figure 2(b). Consistent with perturbation theory [67], T_0 increases linearly with λ for $\lambda \gg 1$.

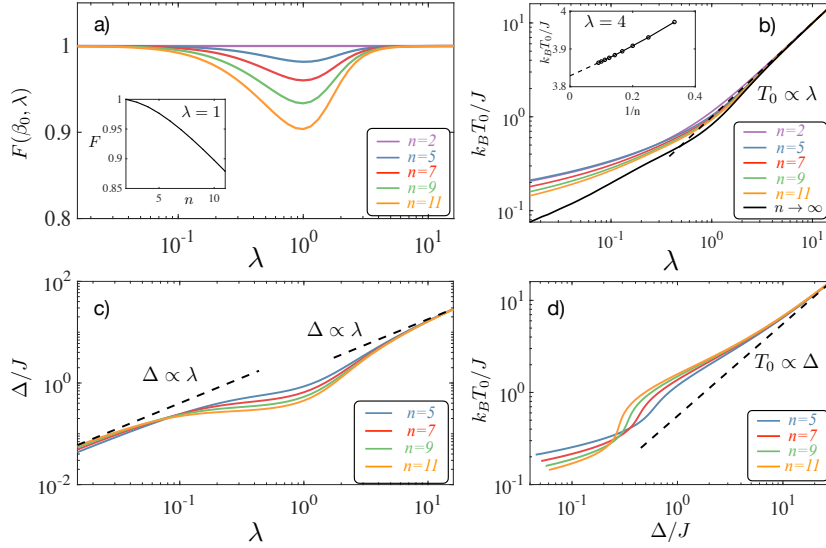


Figure 2. (a) Maximum fidelity $F(\beta_0, \lambda) = \max_{\beta} F(\beta, \lambda)$ versus inter-leg coupling λ . Inset shows $F(\beta_0, \lambda)$ versus n at $\lambda = 1$. $F(\beta_0, \lambda) \gtrsim 0.88$ for $n \leq 11$. (b) Effective temperature T_0 , where the fidelity is maximum, versus inter-leg coupling λ . We extrapolate T_0 to $n \rightarrow \infty$ by doing a linear fit of T_0 versus $1/n$. Inset shows this extrapolation for $\lambda = 4$. (c) The many-body energy gap Δ of H_{parent} versus λ . The gap scales linearly with λ except in a region around $\lambda = 1$. (d) The effective temperature T_0 versus the gap Δ .

3.4. Conformal field theory perspective

A complementary explanation for why the ground state of H_{parent} [(8)] provides a good approximation of the TFD can be given using conformal field theory (CFT), using the results of [68]. In the context of topologically ordered states, the authors of [68] consider two CFTs described by Hamiltonians $H_{L/R}$, coupled by an interaction λH_{LR} that leads to a insulating state with energy gap $\Delta \propto \lambda$. They show that the reduced state, tracing out, e.g., the “ R ” degrees of freedom takes the form $\rho_L \propto e^{-H_L/k_B T}$ with temperature $T \propto \Delta$. For comparison, this is consistent with the construction of the TFD in [63]. An equivalent statement to the above is that the modular Hamiltonian of the ground state of H_{parent} , with respect to the partition of the system into “ L ” and “ R ” degrees of freedom, is given by $H_{L/R}$. This latter observation has been shown to approximately hold for lattice models in several numerical works [67, 69–71].

Our model provides a similar relationship, since we expect the low-energy properties of H , in the thermodynamic limit, to be well described by a CFT. Figure 2(c) plots the gap Δ versus λ , and demonstrates that the approximate relation $\Delta \propto \lambda$ also holds in this case. Note that the fidelity decreases in the region where we observe a deviation from the linear scaling $\Delta \propto \lambda$. For comparison, we also plot T_0 versus Δ in Figure 2(d), and find that $T_0 \propto \Delta$ for large Δ , but it deviates from this linear scaling for $\Delta \lesssim 10J$.

4. Measuring the OTOC from $|g(\lambda)\rangle$

As we said above, since $|g(\lambda)\rangle$ approximates $|\phi(\beta_0)\rangle$, an approximation to the OTOC can be measured by replacing $|\phi(\beta_0)\rangle$ with $|g(\lambda)\rangle$. We denote the measurement $\langle V^\dagger \otimes V^T \rangle$ made with $|g(\lambda)\rangle$ as $O_g(\lambda, t)$. The nonzero infidelity between $|g(\lambda)\rangle$ and $|\phi(\beta_0)\rangle$, for finite $\lambda \neq 0$, yields $O_g(\lambda, t) \neq O_{\text{th}}(\beta_0, t)$. Formally, the error is bounded for all times t by [see Appendix C for proof]

$$\begin{aligned} |O_g(\lambda, t) - O_{\text{th}}(\beta_0, t)| &< 2\|V\|^2 D(|g(\lambda)\rangle, |\phi(\beta_0)\rangle) \\ &= 2\|V\|^2 \sqrt{1 - F(\beta_0, \lambda)} \end{aligned} \quad (13)$$

where $D(|g(\lambda)\rangle, |\phi(\beta_0)\rangle) = \sqrt{1 - F(\beta_0, \lambda)}$ is the trace distance between $|g(\lambda)\rangle$ and $|\phi(\beta_0)\rangle$, and $\|V\|$ is the spectral norm of V . In practice however, the error is much smaller at initial times, and grows with time.

The error at all times is significantly reduced by estimating a corrected OTOC given by

$$O_{\text{corr}}(\lambda, t) \equiv O_g(\lambda, t)/N_g(\lambda, t), \quad (14)$$

where N_g is obtained by performing the measurements with $W = 1$ in the prepared ground state $|g(\lambda)\rangle$. This ratio closely approximates $\tilde{O}_{\text{th}}(\beta_0, t) \equiv O_{\text{th}}(\beta_0, t)/|O_{\text{th}}(\beta_0, 0)|$. The intuitive reason for this is that the nonideality of the initial state, $|g(\lambda)\rangle \neq |\phi(\beta_0)\rangle$, drives similar dynamics in $N_g(\lambda, t)$ and $O_g(\lambda, t)$, and this dynamics is partially canceled in the ratio $O_{\text{corr}}(\lambda, t)$. Then, much of the remaining dynamics in $O_{\text{corr}}(\lambda, t)$ is only due to the scrambling of W . We note that this technique has been successfully applied in earlier works [48, 59, 72] to mitigate errors in measuring the OTOC due to decoherence and noise sources.

4.1. Numerical results for the OTOC

In this section, we demonstrate that (a) $O_g(\lambda, t)$ approximates $O_{\text{th}}(\beta_0, t)$, which is the theoretical OTOC as defined in (1) for inverse temperature β_0 corresponding to the coupling λ , (b) the nontrivial temperature-dependence of $O_{\text{th}}(\beta_0, t)$ is captured well by choosing W and V as Pauli operators on adjacent spins, $W = \sigma_i^\mu$ and $V = \sigma_{i-1}^\nu$, and (c) errors due to non-ideal fidelity for finite $\lambda \neq 0$ are significantly reduced in $O_{\text{corr}}(\lambda, t)$ defined in (14).

Figure 3(b) plots the OTOCs at three different couplings, corresponding to different temperatures [see Figure 2], choosing $W = \sigma_5^z$, $V = \sigma_4^x$, and $n = 8$ as illustrated in Figure 3(a). Dotted lines correspond to $\tilde{O}_{\text{th}}(\beta_0, t) \equiv O_{\text{th}}(\beta_0, t)/O_{\text{th}}(\beta_0, 0)$, dashed lines to $\tilde{O}_g(\lambda, t) \equiv O_g(\lambda, t)/O_g(\lambda, 0)$, and solid lines to $O_{\text{corr}}(\lambda, t) \equiv O_g(\lambda, t)/N_g(\lambda, t)$. The curves start from an initial value of 1 and decay with time. There is good agreement between them throughout most of the decay. The three curves agree exactly at $\lambda = \infty$ (red curves), but finite size effects and the non-ideality of the initial state for the other two couplings introduce a large disagreement between \tilde{O}_{th} and \tilde{O}_g at $Jt/\hbar \gtrsim 0.5$ and $Jt/\hbar \gtrsim 1$. As claimed earlier, the disagreement between \tilde{O}_{th} and O_{corr} is smaller. Shaded

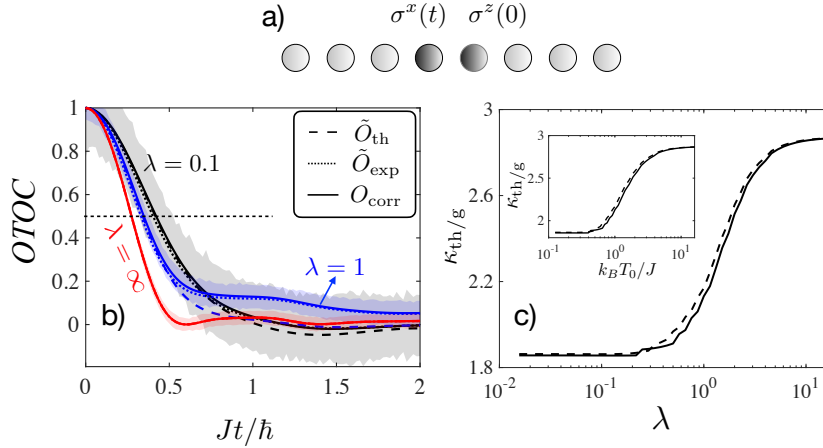


Figure 3. (a) A chain of 8 spins for which we calculate the OTOC for $W = \sigma_5^z$ and $V = \sigma_4^x$. (b) OTOCs $\tilde{O}_g(\lambda, t) = O_g(\lambda, t)/O_g(\lambda, t=0)$ (dashed), $\tilde{O}_{th}(\beta_0, t) = O_{th}(\beta_0, t)/O_{th}(\beta_0, t=0)$ (dotted), and $O_{corr}(\lambda, t) = O_g(\lambda, t)/N_g(\lambda, t)$ (solid), at three different couplings. Shaded areas indicate 1σ statistical error in O_{corr} from 1000 measurements of O_g and N_g at each time. The dashed, dotted, and solid curves coincide at $\lambda = \infty$ (red), but differ for the other two couplings. (c) The slope κ of the curves \tilde{O}_g and \tilde{O}_{th} versus time, at $\tilde{O}_{th} = 0.5$ and $\tilde{O}_g = 0.5$ respectively. κ monotonically increases with coupling λ , and saturates at $\lambda \sim 10$. The inset displays κ as function of temperature $T_0 = T_0(\lambda)$, with $T_0(\lambda) = 1/\beta_0(\lambda)$ determined numerically by maximizing the overlap $F(\beta, \lambda)$ (see main text and Figure 2).

areas plot the 1σ shot noise from 1000 measurements. The shot noise increases as the temperature decreases because the values of O_{th} decrease. The shot noise increases with time for the same reason.

The OTOCs' decay rate is different at the three couplings in Figure 3(b). Figure 3(c) further illustrates this by plotting the slope κ of $\tilde{O}_{th/g}$ (solid/dashed) at $\tilde{O}_{th/g} = 0.5$. This slope monotonically increases with λ and saturates at $\lambda \sim 10$. The inset plots the slope versus T_0 . The fact that the slope, which is a measure of the rate of the OTOC's decay, depends on the state's temperature is a unique feature which has not been experimentally measured before. A key accomplishment of experimentally implementing our protocol would be measuring this temperature-dependence.

Figures 4(a-c) plot the OTOCs for different choices of W and V shown in Figure 4(d), and for different couplings, corresponding to different temperatures [see Figure 2], indicated at the top of each panel.

\tilde{O}_{th} , \tilde{O}_g , and O_{corr} always agree at $\lambda = \infty$ [Figure 4(a)], since our protocol is exact in this case. The OTOC stays nearly constant at $\tilde{O}_g = 1$ for some time before the onset of decay. The time for which it remains nearly constant, $t \sim r/v_B$, is set by the distance r between W and V , and the butterfly velocity v_B [73–75]. This is because the measurement of $V^\dagger \otimes V^T$ at time t is affected only by the neighborhood where the Heisenberg operator $V^\dagger(t) \otimes V^T(t)$ has sufficient support, and this neighborhood grows linearly with time.

\tilde{O}_{th} and \tilde{O}_g disagree for finite $\lambda \neq 0$ [Figure 4(b-c)], and the error is larger when

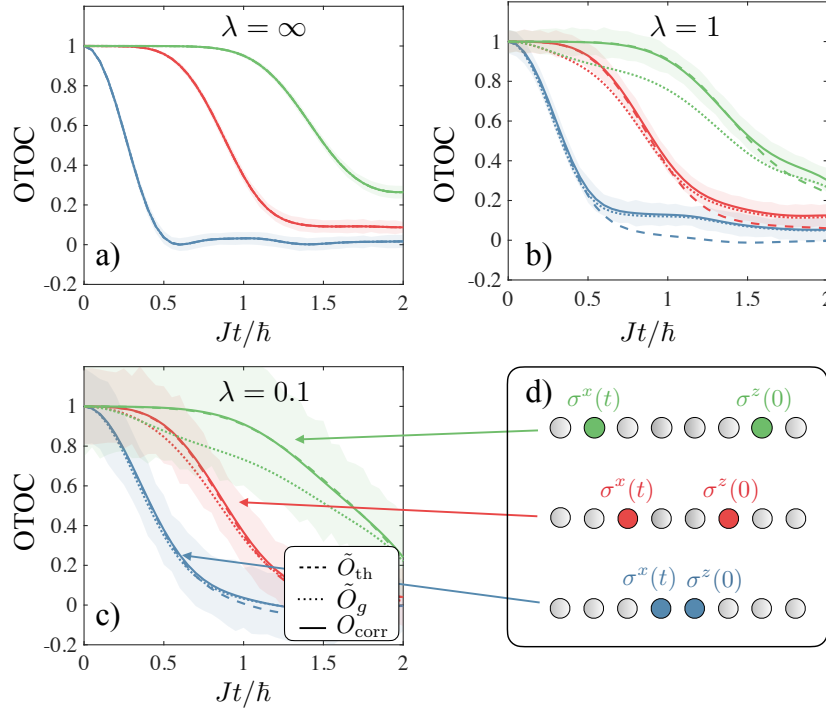


Figure 4. (a-c) OTOCs \tilde{O}_g (dotted), \tilde{O}_{th} (dashed), and O_{corr} (solid) versus time. Each panel considers a different coupling λ . The dotted, dashed, and solid curves coincide at $\lambda = \infty$ (panel a). (d) Choices of W and V in panels (a-c), and their color schemes. Blue lines in (a-c) correspond to $W = \sigma_5^z$ and $V = \sigma_4^x$, red lines to $W = \sigma_6^z$ and $V = \sigma_3^x$, and green lines to $W = \sigma_6^z$ and $V = \sigma_2^x$. $n = 8$ in all cases. Shaded areas indicate 1σ statistical error in O_{corr} from 1000 measurements of O_g and N_g at each time.

W and V are farther apart from each other. Specifically, \tilde{O}_g begins decreasing at $t = 0$ while \tilde{O}_{th} begins decaying at $t \sim r/v_B$ as explained above. The earlier onset of decay in \tilde{O}_g is because $|g(\lambda)\rangle$ evolves with time since it is not an eigenstate of $H_1 - H_2^*$. The spins in each leg get correlated with each other during this evolution, and consequently the correlation $V^\dagger \otimes V^T$ across the two legs gets weaker. Remarkably, O_{corr} has a much smaller error with \tilde{O}_{th} than the error between \tilde{O}_g and \tilde{O}_{th} .

5. Robustness to experimental errors

Decoherence in the system during time evolution, or other sources of imperfections, can produce errors in \tilde{O}_g , even in the limits $\lambda = 0$ and $\lambda = \infty$ where our protocol is supposed to be exact. We consider a few different error mechanisms in this section. For the Hamiltonian we consider [(7)], we find in all cases except local dephasing that O_{corr} removes these errors at least partially and agrees well with \tilde{O}_{th} . Note that the bound derived for $|O_g - O_{th}|$ [(13)] only considers errors in the initial state, and is not valid for the error mechanisms in this section.

The first source of decoherence we consider is collective dephasing, caused by

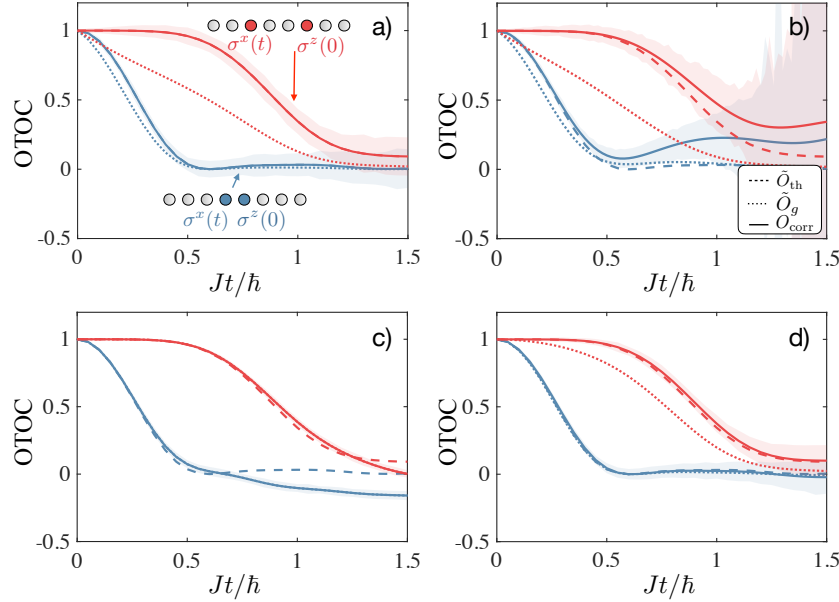


Figure 5. OTOCs \tilde{O}_g (dotted), \tilde{O}_{th} (dashed), and O_{corr} (solid) versus time, in the presence of four error sources. We set $\lambda = \infty$ and $n = 8$. (a) considers depolarization with $\gamma = J$. (b) considers local dephasing with $\gamma = J/4$. (c) considers interaction ϵH_{12} between the two legs during time evolution, with strength $\epsilon = 0.5$. (d) considers the two legs evolving with unequal Hamiltonians $(1 \pm \epsilon)H$, with $\epsilon = 0.2$. Blue lines correspond to $W = \sigma_5^z$ and $V = \sigma_4^x$, and red lines to $W = \sigma_6^z$ and $V = \sigma_3^x$, as shown in the two spin chains in (a). Shaded areas indicate 1σ statistical error in O_{corr} from 1000 measurements of O_g and N_g at each time.

fluctuations in the global magnetic field. We model collective dephasing with the Lindblad equation

$$\hbar \partial_t \rho = -i[H_1 - H_2^*, \rho] - \gamma \left(\sigma_{tot}^z \rho \sigma_{tot}^z - \frac{1}{2} ((\sigma_{tot}^z)^2 \rho + \rho (\sigma_{tot}^z)^2) \right), \quad (15)$$

where $\sigma_{tot}^z = \sum_{i=1}^{2n} \sigma_i^z$, and $\rho(\lambda, 0) = |g(\lambda)\rangle \langle g(\lambda)|$ for the normalization N_g and $\rho(\lambda, 0) = W |g(\lambda)\rangle \langle g(\lambda)| W^\dagger$ for O_g . Remarkably, N_g is completely robust to global dephasing, because $|g(\lambda)\rangle$ is an eigenstate of σ_{tot}^z with eigenvalue 0 for all λ , and $H_1 - H_2^*$ preserves σ_{tot}^z . Thus, the system always lies in a decoherence-free subspace and is insensitive to field fluctuations. O_g is also completely robust to global fluctuations for any W that commutes with σ_{tot}^z , e.g., $W = \sigma_i^z$. A similar argument in the Heisenberg picture also implies that O_g is completely robust to collective dephasing if $V^\dagger \otimes V^T$ commutes with σ_{tot}^z , e.g., $V = \sigma_i^z$.

The second source of decoherence we consider is depolarization, caused by random collective spin flips along all directions. We model depolarization with the Lindblad equation

$$\hbar \partial_t \rho = -i[H_1 - H_2^*, \rho] - \gamma \left(\rho - \frac{1}{4^n} \right). \quad (16)$$

This equation has the solution

$$\rho(\lambda, t) = e^{-i(H_1 - H_2^*)t/\hbar} \rho e^{-i(H_1 - H_2^*)t/\hbar} e^{-\gamma t} + (1 - e^{-\gamma t})/4^n. \quad (17)$$

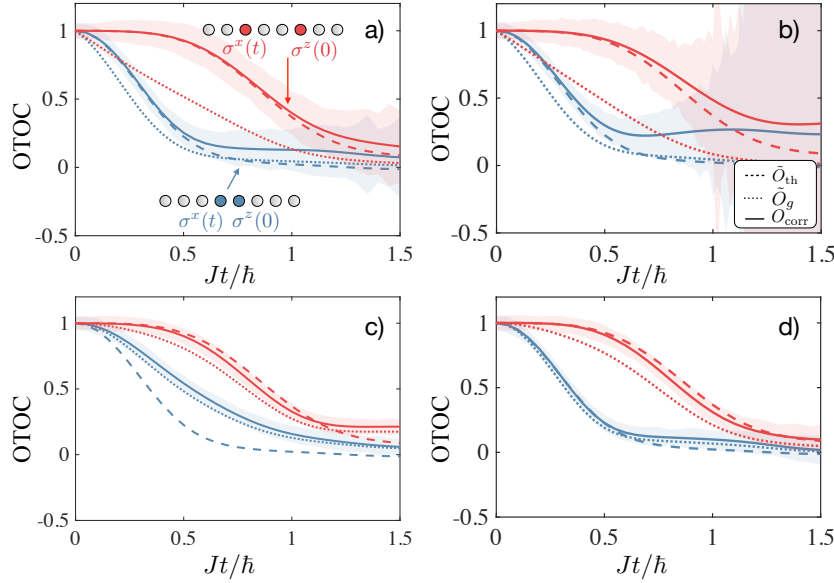


Figure 6. OTOCs \tilde{O}_g (dotted), \tilde{O}_{th} (dashed), and O_{corr} (solid) versus time, in the presence of four error sources. We set $\lambda = 1$ and $n = 8$. (a) considers depolarization with $\gamma = J$. (b) considers local dephasing with $\gamma = J/4$. (c) considers interaction ϵH_{12} between the two legs during time evolution, with strength $\epsilon = 0.5$. (d) considers the two legs evolving with unequal Hamiltonians $(1 \pm \epsilon)H$, with $\epsilon = 0.2$. Blue lines correspond to $W = \sigma_5^z$ and $V = \sigma_4^x$, and red lines to $W = \sigma_6^z$ and $V = \sigma_3^x$, as shown in the two spin chains in (a). Shaded areas indicate 1σ statistical error in O_{corr} from 1000 measurements of O_g and N_g at each time.

It is then straightforward to show that

$$\begin{aligned} N_g(\lambda, t; \gamma) &= e^{-\gamma t} N_g(\lambda, t; \gamma = 0), \\ O_g(\lambda, t; \gamma) &= e^{-\gamma t} O_g(\lambda, t; \gamma = 0). \end{aligned} \quad (18)$$

Our protocol is completely robust to depolarization as well, because the factor $e^{-\gamma t}$ in O_g and N_g cancel each other to give the correct value for O_{corr} .

Figures 5(a) and 6(a) illustrate this robustness to depolarization, at $\lambda = \infty$ and $\lambda = 1$, and $\gamma = J$ in both cases. At $\lambda = \infty$, $O_{corr} = \tilde{O}_{th}$ exactly. At $\lambda = 1$, $O_{corr} \neq \tilde{O}_{th}$ because of the finite infidelity of $|g(\lambda)\rangle$ with $|\phi(\beta_0)\rangle$, but no additional errors are introduced by depolarization. The only effect of depolarization on O_{corr} in both cases is that the shot noise is larger than the one in the case of $\gamma = 0$. This is because the two factors O_g and N_g in the ratio $O_{corr} = O_g/N_g$ are separately measured in experiment, and each factor has a smaller value with depolarization than without. The smaller values lead to a larger shot noise that increases exponentially with γ .

The third source of decoherence we consider is local dephasing, caused by magnetic field fluctuations on each spin. We model local dephasing with the Lindblad equation

$$\hbar \partial_t \rho = -i[H_1 - H_2^*, \rho] - \gamma \sum_{i=1}^{2n} (\sigma_i^z \rho \sigma_i^z - \rho), \quad (19)$$

Figures 5(b) and 6(b) plot \tilde{O}_{th} (dashed), \tilde{O}_g (dotted) and O_{corr} (solid) at $\lambda = \infty$ and

$\lambda = 1$, and $\gamma = J/4$ in both cases. We see a large disagreement between \tilde{O}_{th} and \tilde{O}_g , and a smaller but significant disagreement \tilde{O}_{th} and O_{corr} .

The fourth and fifth error mechanisms we consider are caused by imperfections in the unitary evolution. In Figures 5(c) and 6(c), we consider the case that the coupling between the ladder's two legs is not completely turned off during the time evolution, but there is a remnant coupling ϵH_{12} with $\epsilon = 0.5$. In Figures 5(d) and 6(d), we consider the case that the ladder's two legs have different intra-leg interaction strengths, i.e. they evolve with $(1 - \epsilon)H_1 - (1 + \epsilon)H_2^*$. We set $\epsilon = 0.2$. At $\lambda = \infty$, O_{corr} agrees well with \tilde{O}_{th} for both the error mechanisms. The agreement between them is poorer at $\lambda = 1$.

In addition to mitigating errors due to imperfections in the initial state ($F(\beta_0, \lambda) < 1$), and due to decoherence during time evolution, O_{corr} also corrects errors in measurement. This is the sixth source of error we consider. If the ideal probability to measure $V^\dagger \otimes V^T$ as $(\pm 1, \pm 1)$ after time evolution is $P_{\pm 1, \pm 1}$, and the error probability for each measurement is x , then the ideal and incorrect expectation values of $V^\dagger \otimes V^T$ are respectively

$$\begin{aligned} \langle V^\dagger \otimes V^T \rangle_{\text{ideal}} &= \sum_{\sigma_1, \sigma_2 = \pm 1} \sigma_1 \sigma_2 P_{\sigma_1, \sigma_2}, \\ \langle V^\dagger \otimes V^T \rangle_{\text{incorrect}} &= \sum_{\sigma_1, \sigma_2 = \pm 1} \sigma_1 \sigma_2 \left((1 - x)^2 P_{\sigma_1, \sigma_2} + x(1 - x)(P_{\sigma_1, -\sigma_2} + P_{-\sigma_1, \sigma_2}) \right. \\ &\quad \left. + x^2 P_{-\sigma_1, -\sigma_2} \right). \end{aligned} \quad (20)$$

Simplifying the second line of (20) gives

$$\langle V^\dagger \otimes V^T \rangle_{\text{incorrect}} = (1 - 2x)^2 \langle V^\dagger \otimes V^T \rangle_{\text{ideal}}. \quad (21)$$

Thus, readout errors rescale the ideal expectation value by $(1 - 2x)^2$, in both the factors O_g and N_g . The ratio O_{corr} completely removes readout errors.

6. Connections to earlier works

At infinite temperature, our proposed method is related to two protocols presented earlier in Refs. [48, 49]. These have been experimentally implemented to measure the infinite-temperature OTOC in trapped ion quantum simulators [59, 60].

In Refs. [48, 59], a protocol which employed statistical correlations of randomized measurements to measure the infinite-temperature OTOC was described and realized. Based on correlating separate (sequential) experimental runs, which are initialized in randomized product states and evolved forward in time, it requires only single instances of the n -qubit quantum system. The key idea is to rewrite $O_{\text{th}}(\beta = 0, t)$ as

$$O_{\text{th}}(\beta = 0, t) = \text{tr}(\text{SWAP} \cdot W^\dagger V^\dagger(t) W \otimes V(t)) / 2^n. \quad (22)$$

with $\text{SWAP} = \sum_{\vec{x}, \vec{x}'} |\vec{x}\rangle \langle \vec{x}'| \otimes |\vec{x}'\rangle \langle \vec{x}|$ where the sum runs over all computational basis states $|\vec{x}\rangle$, parametrized by bit strings $\vec{x} = (x_i)_{i=1, \dots, n}$ with $x_i = 0, 1$. As shown in [48], the crux of the method consists in effectively realizing the *two-copy observable* $\text{SWAP}/4^n$ as

an average of randomized initial product states *on single copies* which can be prepared in separate (sequential) experimental runs,

$$\frac{\text{SWAP}}{4^n} = \sum_{\vec{x}} (-2)^{-|\vec{x}|} \overline{(u |\vec{x}\rangle \langle \vec{x}| u^\dagger) \otimes (u |\vec{0}\rangle \langle \vec{0}| u^\dagger)}. \quad (23)$$

Here, $|\vec{x}| \equiv \sum_i x_i$ and the overline denotes the average over local random unitaries $u = \bigotimes_{i=1,\dots,n} u_i$, with u_i sampled independently for each spin from unitary 2 designs [48]. The OTOC is then measured by evolving the system, initialized in the randomized product states $(u |\vec{x}\rangle \langle \vec{x}| u^\dagger)$ forward in time and measure the operators $W^\dagger V^\dagger(t)W$ and $V(t)$, respectively. We note that in practice, the sum in (23) can be truncated to obtain a rapidly converging series of modified OTOCs [48].

The SWAP operator is not positive semi-definite, i.e. it is not a density matrix describing a quantum state. The connection to our protocol can however be understood by mathematically applying a transpose operation to qubits $[n+1, 2n]$ in (23). This yields [76, 77]

$$\frac{|\text{tfd}(\beta=0)\rangle \langle \text{tfd}(\beta=0)|}{2^n} = \sum_{\vec{x}} (-2)^{-|\vec{x}|} \overline{(u |\vec{x}\rangle \langle \vec{x}| u^\dagger) \otimes (u^* |\vec{0}\rangle \langle \vec{0}| u^T)}, \quad (24)$$

where u^T and u^* are respectively the transpose and complex conjugate of u . The infinite-temperature state $|\text{tfd}(\beta=0)\rangle \langle \text{tfd}(\beta=0)|$ can thus be effectively realized as an average over correlated random initial states, prepared by applying u and u^* to bit strings $|\vec{x}\rangle$ and $|\vec{0}\rangle$ in two separate (sequential) runs of the experiment [76, 77].

In the present work, we propose to physically realize $|\text{tfd}(\beta=0)\rangle \langle \text{tfd}(\beta=0)|$ as a pure quantum state on two copies of the systems ($2n$ qubits). As described in Section 2, the OTOC is then measured by evolving the first copy with H and the second copy with $-H^*$, to measure the operator $W^\dagger V^\dagger(t)W \otimes (V(t))^T$, with

$$\begin{aligned} (V(t))^T &= \exp(-iH^T t) V^T \exp(iH^T t) \\ &= \exp(-iH^* t) V^T \exp(iH^* t). \end{aligned} \quad (25)$$

In summary, the quantum protocol for OTOC measurements presented in this work requires twice the number of qubits as the randomized protocol, and requires fine-tuning to realize time evolution with $-H^* = R^\dagger H R$. It can however be readily extended to arbitrary finite temperatures, by preparing finite temperature TFDs $|\text{tfd}(\beta)\rangle \langle \text{tfd}(\beta)|$, and also requires fewer measurements than the randomized protocol in general.

A previous quantum protocol to measure the infinite-temperature OTOC was implemented in [60], following [49]. There, the authors prepared $2n$ qubits in $|\text{tfd}(\beta=0)\rangle$, and one additional independent qubit. Then they evolved the two sets of n qubits independently, similar to our method, and finally measured two qubits in the Bell basis. Because of this measurement basis, they could extract the sum of OTOCs $\sum_{W,V} \text{tr}(W^\dagger V^\dagger(t)W V(t)) / (16 \cdot 2^n)$, where the sum runs over the three Pauli operators and the identity for a spin. The sum of these OTOCs is related to the probability that the initially independent qubit teleported from its initial location to a final location.

Thus, our protocols are identical at $\beta = 0$, except for the presence of the initially independent qubit and choice of the final measurement basis.

We also briefly comment that a previous work [53] proposed a method to measure a differently regularized finite-temperature OTOC [see Appendix A]. In this work, the authors sample $2n$ qubits from thermal ensembles and measures overlap between the qubits after coupling to an ancilla and time evolution. We note that this method does not require sign reversal of the Hamiltonian. Ref. [48] proposed a method to measure a symmetrized variant of the finite-temperature OTOC [see Appendix A] at high temperature. In this protocol, the finite-temperature correction to the infinite-temperature OTOC is obtained via statistical correlations between randomized measurements with global random unitaries.

7. Discussion & Conclusion

We described an experimentally feasible protocol to measure a system's finite-temperature out-of-time-ordered correlation, which is a quantitative probe of the nature of information scrambling. Our method utilizes earlier ideas to prepare the thermofield double state ($|\text{tfd}(\beta)\rangle$) [18, 63], and measure the thermal OTOC from $|\text{tfd}(\beta)\rangle$ [62]. It is geared towards analog quantum simulators with a Hamiltonian respecting particle-hole symmetry and satisfying the ETH, but can also be realized in digital quantum simulators. As an example, we considered the long-ranged XX model that was recently realized in [13], and our protocol can be extended to other models. We access the finite temperature state as one half of $|\text{tfd}(\beta)\rangle$ which is related to the ground state of a local Hamiltonian acting on two copies of the system. For the example we considered, the ground state on two copies of the system well-approximated the desired state for moderate system sizes. In a digital quantum simulator, $|\text{tfd}(\beta)\rangle$ may be prepared variationally for small systems [65, 66]. The OTOC can be obtained by measuring local correlations between two halves of the system, after applying a local perturbation and evolving the two halves independently. We described a protocol to mitigate some errors in the OTOC – those that may arise from, e.g., initial state errors due to finite fidelity with the desired initial state or errors during dynamics such as dephasing – by normalizing the obtained result of this experiment with a second experiment where the initial perturbation is not applied. All the steps described above are realizable in present day quantum simulators.

We also discussed connections between our method at $T = \infty$ and methods adopted in earlier experiments [59, 60]. Applying our method in finite temperature systems with a maximally scrambling Hamiltonian will provide a rigorous test for analytical predictions about information scrambling in these systems [23, 24]. Our method can be straightforwardly applied in systems where the Hamiltonian's sign can be reversed in experiment explicitly, and in systems with a particle-hole symmetric Hamiltonian where explicitly reversing the Hamiltonian's sign will not be necessary. New algorithms are needed for systems where neither of these are true.

Our method goes beyond the paradigm of the infinite temperature OTOC measured in experiments earlier [59, 60], and could lead to the first experimental measurement of the finite-temperature OTOC. The TFD has been of interest in quantum gravity in the context of wormhole teleportation [78–80]. Recently, this teleportation through wormhole has been shown to be thought of as information scrambling in a coupled chain of qubits [81]. Our work can set a useful benchmark via the measurement of thermal OTOCs for such ‘quantum gravity in lab’ ideas [82, 83].

Acknowledgments

Work in Innsbruck was supported by the innovation program under the Grant Agreement No. 731473 (FWF QuantERA via QTFLAG I03769), from the Austrian Science Foundation (FWF, P 32597 N) and by the Simons Collaboration on UltraQuantum Matter, which is a grant from the Simons Foundation (651440, P.Z.). A.E. acknowledges funding by the German National Academy of Sciences Leopoldina under the grant number LPDS 2021-02.

We thank Ana Maria Rey and Murray Holland for a careful reading of the manuscript. We thank Norbert Linke, Alaina Green, and Benoit Vermersch for valuable discussions and comments on the manuscript.

References

- [1] Rainer Blatt and Christian F Roos. Quantum simulations with trapped ions. *Nat. Phys.*, 8(4):277–284, 2012.
- [2] Chris Monroe, Wes C Campbell, Lu-Ming Duan, Z-X Gong, Alexey V Gorshkov, P W Hess, R Islam, K Kim, Norbert M Linke, Guido Pagano, et al. Programmable quantum simulations of spin systems with trapped ions. *Rev. Mod. Phys.*, 93(2):025001, 2021.
- [3] Christian Gross and Immanuel Bloch. Quantum simulations with ultracold atoms in optical lattices. *Science*, 357(6355):995–1001, 2017.
- [4] Antoine Browaeys and Thierry Lahaye. Many-body physics with individually controlled rydberg atoms. *Nat. Phys.*, 16(2):132–142, 2020.
- [5] Morten Kjaergaard, Mollie E Schwartz, Jochen Braumüller, Philip Krantz, Joel I-J Wang, Simon Gustavsson, and William D Oliver. Superconducting qubits: Current state of play. *Annu. Rev. Condens. Matter Phys.*, 11:369–395, 2020.
- [6] Lieven M K Vandersypen and Isaac L Chuang. Nmr techniques for quantum control and computation. *Rev. Mod. Phys.*, 76(4):1037, 2005.
- [7] Jonathan A Jones. Quantum computing with nmr. *Prog. NMR Spectrosc.*, 59:91–120, 2011.
- [8] Ivan Oliveira, Roberto Sarthour Jr, Tito Bonagamba, Eduardo Azevedo, and Jair C C Freitas. *NMR quantum information processing*. Elsevier, 2011.
- [9] Hui Sun, Bing Yang, Han-Yi Wang, Zhao-Yu Zhou, Guo-Xian Su, Han-Ning Dai, Zhen-Sheng Yuan, and Jian-Wei Pan. Realization of a bosonic antiferromagnet. *arXiv preprint arXiv:2009.01426*, 2020.
- [10] Peter T Brown, Debayan Mitra, Elmer Guardado-Sanchez, Reza Nourafkan, Alexis Reymbaut, Charles-David Hébert, Simon Bergeron, A-MS Tremblay, Jure Kokalj, David A Huse, et al. Bad metallic transport in a cold atom fermi-hubbard system. *Science*, 363(6425):379–382, 2019.
- [11] Matthew A Nichols, Lawrence W Cheuk, Melih Okan, Thomas R Hartke, Enrique Mendez,

- T Senthil, Ehsan Khatami, Hao Zhang, and Martin W Zwierlein. Spin transport in a mott insulator of ultracold fermions. *Science*, 363(6425):383–387, 2019.
- [12] Anton Mazurenko, Christie S Chiu, Geoffrey Ji, Maxwell F Parsons, Márton Kanász-Nagy, Richard Schmidt, Fabian Grusdt, Eugene Demler, Daniel Greif, and Markus Greiner. A cold-atom fermi–hubbard antiferromagnet. *Nature*, 545(7655):462–466, 2017.
- [13] Sylvain de Léséleuc, Vincent Lienhard, Pascal Scholl, Daniel Barredo, Sebastian Weber, Nicolai Lang, Hans Peter Büchler, Thierry Lahaye, and Antoine Browaeys. Observation of a symmetry-protected topological phase of interacting bosons with rydberg atoms. *Science*, 365(6455):775–780, 2019.
- [14] Pascal Scholl, Michael Schuler, Hannah J Williams, Alexander A Eberharter, Daniel Barredo, Kai-Niklas Schymik, Vincent Lienhard, Louis-Paul Henry, Thomas C Lang, Thierry Lahaye, Andreas M Läuchli, and Antoine Browaeys. Programmable quantum simulation of 2d antiferromagnets with hundreds of rydberg atoms. *arXiv preprint arXiv:2012.12268*, 2020.
- [15] Sepehr Ebadi, Tout T Wang, Harry Levine, Alexander Keesling, Giulia Semeghini, Ahmed Omran, Dolev Bluvstein, Rhine Samajdar, Hannes Pichler, Wen Wei Ho, et al. Quantum phases of matter on a 256-atom programmable quantum simulator. *arXiv preprint arXiv:2012.12281*, 2020.
- [16] Giulia Semeghini, Harry Levine, Alexander Keesling, Sepehr Ebadi, Tout T Wang, Dolev Bluvstein, Ruben Verresen, Hannes Pichler, Marcin Kalinowski, Rhine Samajdar, et al. Probing topological spin liquids on a programmable quantum simulator. *arXiv preprint arXiv:2104.04119*, 2021.
- [17] Christian Kokail, Christine Maier, Rick van Bijnen, Tiff Brydges, Manoj K Joshi, Petar Jurcevic, Christine A Muschik, Pietro Silvi, Rainer Blatt, Christian F Roos, and Peter Zoller. Self-verifying variational quantum simulation of lattice models. *Nature*, 569(7756):355–360, 2019.
- [18] William Cottrell, Ben Freivogel, Diego M Hofman, and Sagar F Lokhande. How to build the thermofield double state. *J. High Ener. Phys.*, 2019(2):58, 2019.
- [19] Brian Swingle. Unscrambling the physics of out-of-time-order correlators. *Nat. Phys.*, 14(10):988–990, 2018.
- [20] Akram Touil and Sebastian Deffner. Quantum scrambling and the growth of mutual information. *Quantum Sci. Technol.*, 5(3):035005, 2020.
- [21] Nima Lashkari, Douglas Stanford, Matthew Hastings, Tobias Osborne, and Patrick Hayden. Towards the fast scrambling conjecture. *J. High Energy Phys.*, 2013(4):22, 2013.
- [22] Stephen H Shenker and Douglas Stanford. Multiple shocks. *J. High Energy Phys.*, 2014(12):46, 2014.
- [23] Juan Maldacena, Stephen H Shenker, and Douglas Stanford. A bound on chaos. *J. High Energy Phys.*, 2016(8):106, 2016.
- [24] Chaitanya Murthy and Mark Srednicki. Bounds on chaos from the eigenstate thermalization hypothesis. *Phys. Rev. Lett.*, 123(23):230606, 2019.
- [25] Daniel A. Roberts and Douglas Stanford. Diagnosing chaos using four-point functions in two-dimensional conformal field theory. *Phys. Rev. Lett.*, 115:131603, Sep 2015.
- [26] Pavan Hosur, Xiao-Liang Qi, Daniel A Roberts, and Beni Yoshida. Chaos in quantum channels. *J. High Energy Phys.*, 2016(2):4, 2016.
- [27] Xiao Chen, Tianci Zhou, David A Huse, and Eduardo Fradkin. Out-of-time-order correlations in many-body localized and thermal phases. *Annalen der Physik*, 529(7):1600332, 2017.
- [28] Koji Hashimoto, Keiju Murata, and Ryosuke Yoshii. Out-of-time-order correlators in quantum mechanics. *J. High Energy Phys.*, 2017(10):138, 2017.
- [29] C. W. von Keyserlingk, Tibor Rakovszky, Frank Pollmann, and S. L. Sondhi. Operator hydrodynamics, otocs, and entanglement growth in systems without conservation laws. *Phys. Rev. X*, 8:021013, Apr 2018.
- [30] Yunxiang Liao and Victor Galitski. Nonlinear sigma model approach to many-body quantum chaos: Regularized and unregularized out-of-time-ordered correlators. *Phys. Rev. B*, 98:205124, 2018.

Nov 2018.

- [31] Juan Maldacena and Douglas Stanford. Remarks on the sachdev-ye-kitaev model. *Phys. Rev. D*, 94:106002, Nov 2016.
- [32] Douglas Stanford. Many-body chaos at weak coupling. *J. High Energy Phys.*, 2016(10):9, 2016.
- [33] Aavishkar A. Patel, Debanjan Chowdhury, Subir Sachdev, and Brian Swingle. Quantum butterfly effect in weakly interacting diffusive metals. *Phys. Rev. X*, 7:031047, Sep 2017.
- [34] Ron Belyansky, Przemyslaw Bienias, Yaroslav A. Kharkov, Alexey V. Gorshkov, and Brian Swingle. A minimal model for fast scrambling. *Phys. Rev. Lett.*, 125:130601, 2020.
- [35] Zehan Li, Sayan Choudhury, and W. Vincent Liu. Fast scrambling without appealing to holographic duality. *Phys. Rev. Res.*, 2:043399, Dec 2020.
- [36] Sagar Vijay and Ashvin Vishwanath. Finite-temperature scrambling of a random hamiltonian, 2018.
- [37] Bryce Kobrin, Zhenbin Yang, Gregory D. Kahanamoku-Meyer, Christopher T. Olund, Joel E. Moore, Douglas Stanford, and Norman Y. Yao. Many-body chaos in the sachdev-ye-kitaev model. *Phys. Rev. Lett.*, 126:030602, Jan 2021.
- [38] Paul Romatschke. Quantum mechanical out-of-time-ordered-correlators for the anharmonic (quartic) oscillator. *J. High Energy Phys.*, 2021(1):30, 2021.
- [39] Robert J Lewis-Swan, Sean R Muleady, and Ana Maria Rey. Detecting out-of-time-order correlations via quasiadiabatic echoes as a tool to reveal quantum coherence in equilibrium quantum phase transitions. *Phys. Rev. Lett.*, 125(24):240605, 2020.
- [40] Xinfang Nie, Bo-Bo Wei, Xi Chen, Ze Zhang, Xiuzhu Zhao, Chudan Qiu, Yu Tian, Yunlan Ji, Tao Xin, Dawei Lu, and Jun Li. Experimental observation of equilibrium and dynamical quantum phase transitions via out-of-time-ordered correlators. *Phys. Rev. Lett.*, 124(25):250601, 2020.
- [41] Ceren B Dağ, Kai Sun, and Luming M Duan. Detection of quantum phases via out-of-time-order correlators. *Phys. Rev. Lett.*, 123(14):140602, 2019.
- [42] Ceren B Dağ, Luming M Duan, and Kai Sun. Topologically induced prescrambling and dynamical detection of topological phase transitions at infinite temperature. *Phys. Rev. B*, 101(10):104415, 2020.
- [43] Bo-Bo Wei, Gaoyong Sun, and Myung-Joong Hwang. Dynamical scaling laws of out-of-time-ordered correlators. *Phys. Rev. B*, 100(19):195107, 2019.
- [44] Zheng-Hang Sun, Jia-Qi Cai, Qi-Cheng Tang, Yong Hu, and Heng Fan. Out-of-time-order correlators and quantum phase transitions in the rabi and dicke models. *Ann. Phys. (Leipzig)*, 532(4):1900270, 2020.
- [45] Qian Wang and Francisco Pérez-Bernal. Probing an excited-state quantum phase transition in a quantum many-body system via an out-of-time-order correlator. *Phys. Rev. A*, 100(6):062113, 2019.
- [46] Markus Heyl, Frank Pollmann, and Balázs Dóra. Detecting equilibrium and dynamical quantum phase transitions in ising chains via out-of-time-ordered correlators. *Phys. Rev. Lett.*, 121(1):016801, 2018.
- [47] Huitao Shen, Pengfei Zhang, Ruihua Fan, and Hui Zhai. Out-of-time-order correlation at a quantum phase transition. *Phys. Rev. B*, 96(5):054503, 2017.
- [48] Benoît Vermersch, Andreas Elben, Lukas M Sieberer, Norman Y Yao, and Peter Zoller. Probing scrambling using statistical correlations between randomized measurements. *Phys. Rev. X*, 9(2):021061, 2019.
- [49] Beni Yoshida and Norman Y Yao. Disentangling scrambling and decoherence via quantum teleportation. *Phys. Rev. X*, 9(1):011006, 2019.
- [50] Brian Swingle, Gregory Bentsen, Monika Schleier-Smith, and Patrick Hayden. Measuring the scrambling of quantum information. *Phys. Rev. A*, 94(4):040302(R), 2016.
- [51] Guanyu Zhu, Mohammad Hafezi, and Tarun Grover. Measurement of many-body chaos using a quantum clock. *Phys. Rev. A*, 94(6):062329, 2016.
- [52] Sreeram P G, Naga Dileep Varikuti, and Vaibhav Madhok. Exponential speedup in measuring

- out-of-time-ordered correlators with a single bit of quantum information. *arXiv preprint arXiv:2009.03415*, 2020.
- [53] Norman Y Yao, Fabian Grusdt, Brian Swingle, Mikhail D Lukin, Dan M Stamper-Kurn, Joel E Moore, and Eugene A Demler. Interferometric approach to probing fast scrambling. *arXiv preprint arXiv:1607.01801*, 2016.
- [54] Nicole YungerHalpern. Jarzynski-like equality for the out-of-time-ordered correlator. *Phys. Rev. A*, 95(1):012120, 2017.
- [55] Jun Li, Ruihua Fan, Hengyan Wang, Bingtian Ye, Bei Zeng, Hui Zhai, Xinhua Peng, and Jiangfeng Du. Measuring out-of-time-order correlators on a nuclear magnetic resonance quantum simulator. *Phys. Rev. X*, 7(3):031011, 2017.
- [56] Ken Xuan Wei, Chandrasekhar Ramanathan, and Paola Cappellaro. Exploring localization in nuclear spin chains. *Phys. Rev. Lett.*, 120(7):070501, 2018.
- [57] Xinfang Nie, Ze Zhang, Xiuzhu Zhao, Tao Xin, Dawei Lu, and Jun Li. Detecting scrambling via statistical correlations between randomized measurements on an nmr quantum simulator. *arXiv preprint arXiv:1903.12237*, 2019.
- [58] Martin Gärttner, Justin G Bohnet, Arghavan Safavi-Naini, Michael L Wall, John J Bollinger, and Ana Maria Rey. Measuring out-of-time-order correlations and multiple quantum spectra in a trapped-ion quantum magnet. *Nat. Phys.*, 13(8):781–786, 2017.
- [59] Manoj K Joshi, Andreas Elben, Benoît Vermersch, Tiff Brydges, Christine Maier, Peter Zoller, Rainer Blatt, and Christian F Roos. Quantum information scrambling in a trapped-ion quantum simulator with tunable range interactions. *Phys. Rev. Lett.*, 124:240505, 2020.
- [60] Kevin A Landsman, Caroline Figgatt, Thomas Schuster, Norbert M Linke, Beni Yoshida, Norm Y Yao, and Christopher Monroe. Verified quantum information scrambling. *Nature*, 567(7746):61–65, 2019.
- [61] Xiao Mi, Pedram Roushan, Chris Quintana, Salvatore Mandra, Jeffrey Marshall, Charles Neill, Frank Arute, Kunal Arya, Juan Atalaya, Ryan Babbush, et al. Information scrambling in computationally complex quantum circuits. *arXiv preprint arXiv:2101.08870*, 2021.
- [62] Étienne Lantagne-Hurtubise, Stephan Plugge, Oguzhan Can, and Marcel Franz. Diagnosing quantum chaos in many-body systems using entanglement as a resource. *Phys. Rev. Res.*, 2(1):013254, 2020.
- [63] Juan Maldacena and Xiao-Liang Qi. Eternal traversable wormhole. *arXiv preprint arXiv:1804.00491*, 2018.
- [64] Bhuvanesh Sundar. Proposal to measure out-of-time-ordered correlations using bell states. *arXiv preprint arXiv:2006.15093*, 2020.
- [65] Daiwei Zhu, Sonika Johri, Norbert M Linke, K A Landsman, C Huerta Alderete, Nhung H Nguyen, A Y Matsuura, T H Hsieh, and Chris Monroe. Generation of thermofield double states and critical ground states with a quantum computer. *Proceedings of the National Academy of Sciences*, 117(41):25402–25406, 2020.
- [66] Akhil Francis, Daiwei Zhu, C. Huerta Alderete, Sonika Johri, Xiao Xiao, Jim K. Freericks, Chris Monroe, Norbert M. Linke, and A. F. Kemper. Many body thermodynamics on quantum computers via partition function zeros. *arXiv preprint arXiv:2009.04648*, 2020.
- [67] Ingo Peschel and Ming-Chiang Chung. On the relation between entanglement and subsystem hamiltonians. *EPL (Europhys. Lett.)*, 96(5):50006, 2011.
- [68] Xiao-Liang Qi, Hosho Katsura, and Andreas WW Ludwig. General relationship between the entanglement spectrum and the edge state spectrum of topological quantum states. *Phys. Rev. Lett.*, 108(19):196402, 2012.
- [69] Andreas M Läuchli and John Schliemann. Entanglement spectra of coupled $s = 1/2$ spin chains in a ladder geometry. *Phys. Rev. B*, 85(5):054403, 2012.
- [70] Christian Kokail, Bhuvanesh Sundar, Torsten V Zache, Andreas Elben, Benoît Vermersch, Marcello Dalmonte, Rick van Bijnen, and Peter Zoller. Quantum variational learning of the entanglement hamiltonian. *arXiv preprint arXiv:2105.04317*, 2021.

- [71] Mahdiah Pourjafarabadi, Hanieh Najafzadeh, Mohammad-Sadegh Vaezi, and Abolhassan Vaezi. Entanglement hamiltonian of interacting systems: Local temperature approximation and beyond. *Phys. Rev. Res.*, 3(1):013217, 2021.
- [72] Yong-Liang Zhang, Yichen Huang, and Xie Chen. Information scrambling in chaotic systems with dissipation. *Phys. Rev. B*, 99(1):014303, 2019.
- [73] Daniel A Roberts and Brian Swingle. Lieb-robinson and the butterfly effect in quantum field theories. *Phys. Rev. Lett.*, 117(9):091602, 2016.
- [74] Daniel A Roberts, Douglas Stanford, and Leonard Susskind. Localized shocks. *J. High Energy Phys.*, 2015(3):1–27, 2015.
- [75] Márk Mezei and Douglas Stanford. On entanglement spreading in chaotic systems. *J. High Energy Phys.*, 2017(5):1–24, 2017.
- [76] J. Watrous. *The Theory of Quantum Information*. Cambridge University Press, 2018.
- [77] Andreas Elben, Jinlong Yu, Guanyu Zhu, Mohammad Hafezi, Frank Pollmann, Peter Zoller, and Benoît Vermersch. Many-body topological invariants from randomized measurements in synthetic quantum matter. *Sci. Adv.*, 6(15):eaaz3666, Apr 2020.
- [78] Juan Maldacena. Eternal black hole. *JHEP*, 04:021, 2003.
- [79] Juan Maldacena, Douglas Stanford, and Zhenbin Yang. Diving into traversable wormholes. *Fortschritte der Physik*, 65(5), may 2017.
- [80] Ping Gao, Daniel Louis Jafferis, and Aron C. Wall. Traversable wormholes via a double trace deformation. *J. High Energy Phys.*, 2017(12), dec 2017.
- [81] Thomas Schuster, Bryce Kobrin, Ping Gao, Iris Cong, Emil T. Khabiboulline, Norbert M. Linke, Mikhail D. Lukin, Christopher Monroe, Beni Yoshida, and Norman Y. Yao. Many-body quantum teleportation via operator spreading in the traversable wormhole protocol, 2021.
- [82] Adam R. Brown, Hrant Gharibyan, Stefan Leichenauer, Henry W. Lin, Sepehr Nezami, Grant Salton, Leonard Susskind, Brian Swingle, and Michael Walter. Quantum gravity in the lab: Teleportation by size and traversable wormholes, 2021.
- [83] Sepehr Nezami, Henry W. Lin, Adam R. Brown, Hrant Gharibyan, Stefan Leichenauer, Grant Salton, Leonard Susskind, Brian Swingle, and Michael Walter. Quantum gravity in the lab: Teleportation by size and traversable wormholes, part ii, 2021.
- [84] Michael A Nielsen and Isaac Chuang. *Quantum computation and quantum information*. American Association of Physics Teachers, 2002.

Appendix A. Different definitions of thermal OTOC

Researchers have used various definitions of the thermal OTOC in the literature. These are:

$$\begin{aligned}
 O_1(\beta, t) &= \frac{\text{tr}(y^2 W^\dagger V^\dagger(t) y^2 W V(t))}{\text{tr}(e^{-\beta H})}, \\
 O_2(\beta, t) &= \frac{\text{tr}(y^4 W^\dagger V^\dagger(t) W V(t))}{\text{tr}(e^{-\beta H})}, \\
 O_3(\beta, t) &= \frac{\text{tr}(y W^\dagger y V^\dagger(t) y W y V(t))}{\text{tr}(e^{-\beta H})}, \\
 O_{\text{th}}(\beta, t) &= \frac{\text{tr}(y^2 W^\dagger V^\dagger(t) W y^2 V(t))}{\text{tr}(e^{-\beta H})},
 \end{aligned} \tag{A.1}$$

where $y = e^{-\beta H/4}$. The definition in the last line is used by us in this paper. The above definitions typically show different behaviors from one another for non-maximally-scrambling Hamiltonians at finite temperature. They converge to the same value for

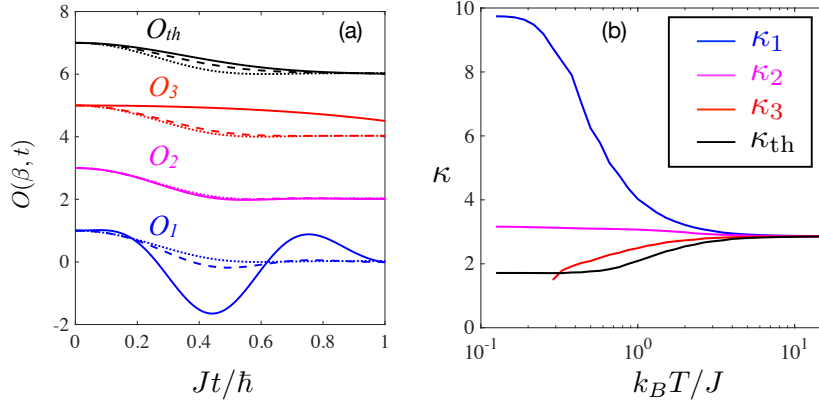


Figure A1. (a) OTOCs $\tilde{O}_{1/2/3/th}(\beta, t)$ and (b) their rates of decay. (a) Blue curves plot $\tilde{O}_1(\beta, t)$, magenta curves are $\tilde{O}_2(\beta, t)$, red curves are $\tilde{O}_3(\beta, t)$, and black curves are $\tilde{O}_{th}(\beta, t)$. Solid, dashed, and dotted lines correspond to $k_B T/J = 1/8, 1$, and 8 respectively. The curves corresponding to the four OTOCs are shifted from one another for clarity. (b) The slope of $\tilde{O}(\beta, t)$ at $\tilde{O}(\beta, t) = 0.5$. The different OTOCs exhibit very different slopes, and even show different trends with temperature. (The curves are unshifted).

$\beta = 0$. Refs. [53] described a quantum algorithm, based on sampling thermal states, to measure $O_2(\beta, t)$, and [62] proposed to measure $O_{th}(\beta, t)$ and $O_1(\beta, t)$ using the thermofield double state. Algorithms to experimentally measure $O_3(\beta, t)$ at arbitrary temperature have not been developed. Here, we investigate their behaviors for the Hamiltonian in (7).

Figure A1(a) plots $\tilde{O}_{1/2/3/th}(\beta, t)$ for nearest-neighbor W and V and different temperatures. All the four kinds of OTOC decay initially with time. But their decay rates are very different from one another. Further, the decay's temperature-dependence is different for the four definitions. While the decay gets steeper as temperature increases for O_{th} and O_3 , it gets less steep for O_2 and is nearly temperature-independent for O_1 . As before, we compute and plot the curves' slopes at $\tilde{O} = 1/2$ in Figure A1(b). The slope κ increases with temperature for O_{th} (Figure 2 and black curve in Figure A1(b)) and O_3 (red curve), decreases with temperature for O_1 (blue curve), and is nearly constant for O_2 (pink curve).

Why these different OTOCs, all of which have been used in the literature, decay at different rates, and what aspects of information scrambling they capture or miss, are intriguing questions for future exploration.

Appendix B. Thermofield double state for $n = 2$

Here, we show that $|g(\lambda)\rangle = |\phi(\beta_0)\rangle$ for $n = 2$. The ground state of $H_{\text{parent}}(\lambda)$ is

$$\begin{aligned}
 |g(\lambda)\rangle = & -\frac{\lambda}{2\sqrt{1+\lambda^2}} (|\uparrow\uparrow\rangle |\downarrow\downarrow\rangle + |\downarrow\downarrow\rangle |\uparrow\uparrow\rangle) \\
 & -\frac{1}{2\sqrt{1+\lambda^2}} (|\uparrow\downarrow\rangle |\uparrow\downarrow\rangle + |\downarrow\uparrow\rangle |\downarrow\uparrow\rangle)
 \end{aligned}$$

$$+ \frac{1}{2} (|\uparrow\downarrow\rangle |\downarrow\uparrow\rangle + |\downarrow\uparrow\rangle |\uparrow\downarrow\rangle). \quad (\text{B.1})$$

Similarly,

$$\begin{aligned} |\phi(\beta)\rangle = & -\frac{1}{2 \cosh \beta} (|\uparrow\uparrow\rangle |\downarrow\downarrow\rangle + |\downarrow\downarrow\rangle |\uparrow\uparrow\rangle) \\ & -\frac{\tanh \beta}{2} (|\uparrow\downarrow\rangle |\uparrow\downarrow\rangle + |\downarrow\uparrow\rangle |\downarrow\uparrow\rangle) \\ & + \frac{1}{2} (|\uparrow\downarrow\rangle |\downarrow\uparrow\rangle + |\downarrow\uparrow\rangle |\uparrow\downarrow\rangle). \end{aligned} \quad (\text{B.2})$$

A straightforward comparison gives $|g(\lambda)\rangle = |\phi(\beta_0)\rangle$ when $\lambda = 1/\sinh \beta_0$.

Appendix C. Upper bound for errors due to the initial state

For any two states ρ and σ , the difference in the expectation value of any operator O can be upper bounded as follows. First, we expand O in its eigen basis $\{|o_\mu\rangle\}$,

$$\langle O \rangle_\rho - \langle O \rangle_\sigma = \sum_\mu o_\mu \langle o_\mu | \rho - \sigma | o_\mu \rangle. \quad (\text{C.1})$$

Using the triangle sum rule,

$$\langle O \rangle_\rho - \langle O \rangle_\sigma \leq \sum_\mu |o_\mu| \langle o_\mu | \rho - \sigma | o_\mu \rangle. \quad (\text{C.2})$$

Then, using $|o_\mu| \leq \|O\|$, with $\|O\|$ being the spectral norm of O , and the definition of the trace distance $D(\rho, \sigma)$, we get

$$\langle O \rangle_\rho - \langle O \rangle_\sigma \leq 2\|O\|D(\rho, \sigma). \quad (\text{C.3})$$

The operator measured in our protocol is $O = V \otimes V^T$, which has spectral norm $\|V\|^2$. This proves the first line in (13), with $\rho = |g(\lambda)\rangle \langle g(\lambda)|$ and $\sigma = |\phi(\beta_0)\rangle \langle \phi(\beta_0)|$. These states are pure states, and a standard property [84] for pure states leads to the second line in (13). The bound is valid for all times, since the spectral norm of a Heisenberg operator is constant with time evolution.